ACS SENSORS

pubs.acs.org/acssensors Article

Microphysiological System for High-Throughput Computer Vision Measurement of Microtissue Contraction

Ana Maria Gracioso Martins, Michael D. Wilkins, Frances S. Ligler, Michael A. Daniele, and Donald O. Freytes*

Cite This: *ACS Sens.* 2021, 6, 985−994 Read Online

ACCESS | Metrics & More | Article Recommendations | Supporting Information

ABSTRACT: The ability to measure microtissue contraction in vitro can provide important information when modeling cardiac, cardiovascular, respiratory, digestive, dermal, and skeletal tissues. However, measuring tissue contraction in vitro often requires the use of high number of cells per tissue construct along with time-consuming microscopy and image analysis. Here, we present an inexpensive, versatile, high-throughput platform to measure microtissue contraction in a 96-well plate configuration using one-step batch imaging. More specifically, optical fiber microprobes are embedded in microtissues, and contraction is measured as a function of the deflection of optical signals emitted from the end of the fibers. Signals can be measured from all the filled wells on the plate simultaneously using a digital camera. An algorithm uses pixel-based image analysis and computer vision techniques for the accurate multiwell quantification of positional changes in the optical microprobes caused by the contraction of the microtissues. Microtissue constructs containing 20,000−100,000 human ventricular cardiac fibroblasts (NHCF-V) in 6 mg/mL collagen type I showed contractile displacements ranging from 20−200 μm. This highly sensitive and versatile platform can be used for the high-throughput screening of microtissues in disease modeling, drug screening for therapeutics, physiology research, and safety pharmacology.

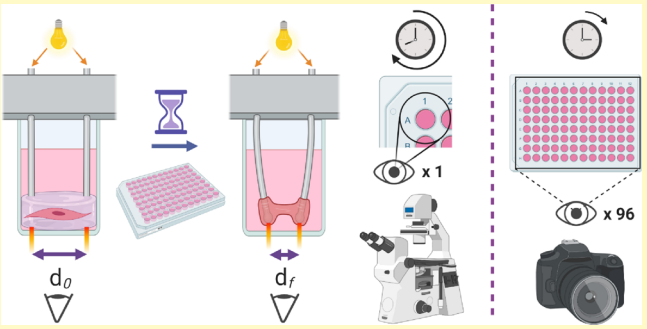

KEYWORDS: *high throughput, 3D culture, tissue function, tissue contraction, computer vision.*

Tissue contraction measurements can be used to study the contractile response of cells and engineered tissues under physiological conditions modeled in vitro.[1] More specifically, the ability to measure microtissue contraction over time can reveal important information about physiological and pathophysiological processes required for disease modeling, drug development, and safety pharmacology studies.[2−6]

In addition to being associated with cardiac, skeletal, and smooth muscle cell activities, tissue contraction is essential to many other processes throughout the body, such as connective tissue morphogenesis, gastrulation, and wound contraction.[7] Tissue contraction not only drives tissue development and homeostasis at the tissue level but also governs functions such as receptor signaling, differentiation, and proliferation at the cellular level.[8]

Tissue contractility is the ability of a tissue to self-contract, whereas tissue contraction is the metric contraction of the tissue itself.[14] As the planar microenvironment of two-dimensional (2D) culture has a direct effect on the cell cytoskeleton and fails to provide the degrees of freedom necessary for a proper mechanical function in vitro,[9] three-dimensional (3D)-engineered tissue constructs provide a superior model of tissue contractility and function as they mimic the native tissue and its microenvironment more closely.[10] Engineered tissue constructs larger than a few microns in all the three dimensions, however, are subject to diffusional limitations of critical nutrients, removal of cellular waste, and exposure to experimental therapeutic factors.[11]

The size limitations on 3D tissues impose serious requirements on measurement systems in terms of accurate experimental setup, highly sensitive imaging methods, and measurement precision.[8,12] As a result, an important requirement for systems to measure the contractility of 3D tissues in vitro is their ability to reliably reproduce and measure tissue contraction at the microscale.[13] Hence, methods to sense and quantify microtissue contraction must be sufficiently sensitive to measure subtle metric contraction in microtissues and yet be flexible enough to cover a wide range of contraction frequencies and motions. Improvements in motion-tracking measurements

Received: October 16, 2020
Accepted: February 10, 2021
Published: March 3, 2021

https://dx.doi.org/10.1021/acssensors.0c02172
ACS Sens. 2021, 6, 985−994

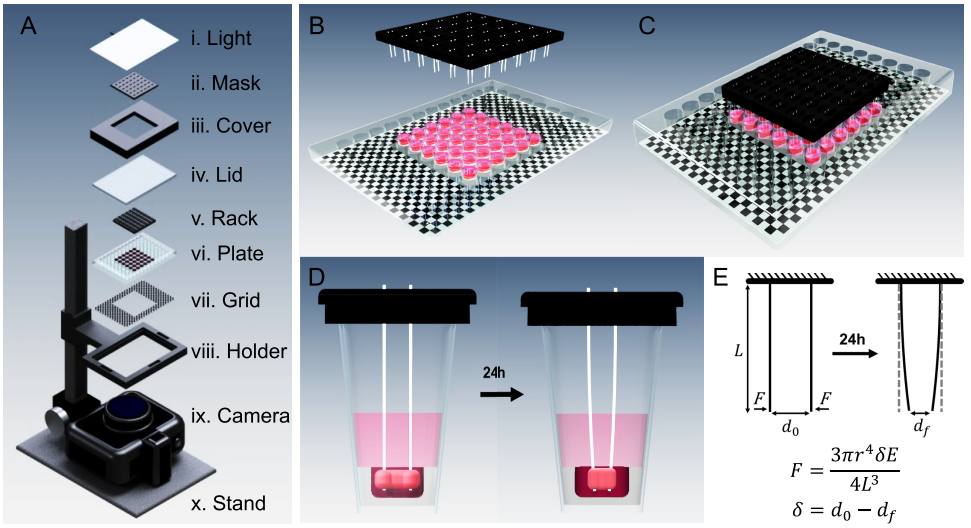

Figure 1. Instrumental configuration—(A) (i). Electroluminescent panel, (ii) slit mask, (iii) Plate cover, (iv) 96-well plate lid, (v) rack fitted with optical fibers, (vi) stamped 96-well plate with microtissues in microwells, (vii) Calibration grid, (viii) Plate holder, (ix) camera, and (x) camera stand. (B) Detailed perspective view of the core experimental components (rack, plate, and grid), (C) Perspective top view of the 96-well plate fitted with the rack containing optical fibers, (D) Graphical representation of how the contraction measurements are obtained in the proposed system: side view of the well containing a microtissue wrapped around the two segments of the optical fiber showing significant contraction and bending of the optical fibers after 24 h. (E) Schematic of the cantilever-beam theory showing the force (F) exerted at the end of a cantilever, with an initial distance d_0 and a final distance d_f, where r = optical fiber radius, δ = optical fiber deflection, E = elastic modulus of the optical fiber, and L = optical fiber length.

could expand the usefulness of microtissue contraction as a high throughput in vitro evaluation tool. Therefore, a sensitive and flexible high-throughput in vitro method to detect contraction efficiently and precisely is needed.

In the US in 2010, the National Institutes of Health and the Food and Drug Administration cofounded the microphysiological systems program to accelerate the development of microphysiological platforms designed to model a minimal set of physiological conditions while incorporating readout tools for monitoring engineered microtissues in vitro.[15] To this end, a wide variety of devices have been developed to model 3D microtissue constructs in vitro.[10,16−21] However, these systems are generally expensive to operate, as they may need sophisticated microfabrication facilities, require a large number of cells per experimental condition, and/or employ high precision imaging systems and software for accurate imaging and quantitation.[5]

A common approach to study the contractile behavior of engineered microtissues is to embed flexible polydimethylsiloxane (PDMS) micropillars into 3D microtissues and indirectly evaluate the forces exerted on the PDMS micropillars as a function of micropillar deflection.[1,5,8,20,22−30] In this configuration, microtissue remodeling is guided by micropillar-defined mechanical boundary conditions.[22,24,31] In such systems, microtissue contraction measurements are obtained via microscopy by imaging each experimental condition individually[5,20,22−27,29,32,33] and measuring the distance between the micropillars either manually (ImageJ[23,24,34]) or with the aid of commercial or open source software (LabView,[1,9] MATLAB,[1,20,27,35] Fiji,[26] and Python[22]). In other instances, the measurements of micropillar deflection are performed using custom-made imaging hardware and software.[5,23,28,32] Details on analogous platforms can be found in the Supporting Information (SI) Tables S1 and S2.

Even though some of these noncustomized methods claim to be high-throughput systems compatible with 12-,[24] 24-,[35] 48−[34] and 96−[1,19,22,36] well plates, the need to image one individual well at a time renders them low-throughput and time-consuming. Most importantly, accurately detecting PDMS micropillars embedded in microtissues can be a visually challenging task as microtissues encapsulate the micropillars and microtissue−micropillar boundaries may not be clearly defined. Tracking an object that is subject to change in appearance through occlusion of pillars, changes in the tissue shape, variations in illumination, and—in some instances—motion blur is a major challenge for both a human operator and an object-tracking software.[37] Although object-tracking software has evolved to work around these physical challenges, complex quasi-physical solutions such as point cloud processing through stereo imaging, 3D scanning, feature-based registration, and iterative closest-point algorithm processing in an effort to reconstruct the tracked object in 3D[38] may not be sufficiently accurate for tissue engineering applications as biological samples express a large number of nontrivial variations.[39] Hence, an accurate high-throughput method featuring a physical marker that offers high definition between tissues and micropillar boundaries is highly desirable.

Here, we introduce the use of optical fiber microprobes as flexible, high-definition physical markers to accurately measure microtissue contraction remotely via batch camera image analysis using computer vision. We demonstrate that 3D microtissue contraction can be accurately quantified via microscopy and camera-imaging methods by measuring the deflection of optical fiber microprobes embedded in microtissues composed of human cardiac fibroblasts of ventricular origin (NHCF-V) in a 3D collagen matrix. The platform images the microtissues simultaneously in multiple microwells via a camera placed at the bottom of the wells. The clear definition of the fiber probes within the microscale tissues enables the simultaneous measurement of tissue contraction using batch 2D image analysis with reduced processing power requirements compared to 3D techniques. The work reported here presents a complete, versatile, and inexpensive method to fabricate

https://dx.doi.org/10.1021/acssensors.0c02172
ACS Sens. 2021, 6, 985−994

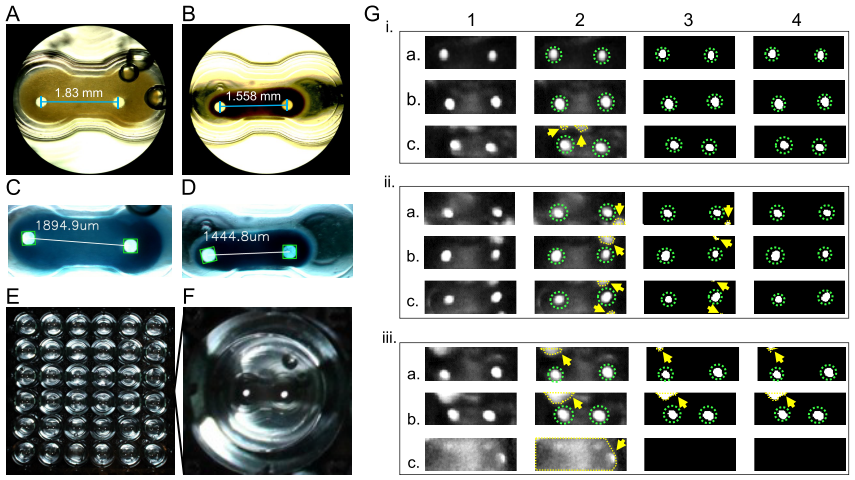

Figure 2. Image capture and processing. (A) Hand-annotated microscopy images showing center-to-center measurements at zero (1.83 mm) and (B) 48 h (1.558 mm) for a microtissue containing 100,000 cells. (C) Example of bounding boxes after the object detection of each optical fiber and the resulting measurement of centroid distance converted to mm at zero (1.8949 mm) and (D) 24 h (1.4448 mm). (E) SLR camera image obtained at 20 cm from the bottom of the plate, (F) magnified sample well (not to scale), (G) graphical output of the camera image-processing steps showing grayscale image conversion and cropping (1) and thresholding iterations (2−4) to eliminate artifacts in the wells. Dotted green lines highlight the optical fibers, whereas dotted yellow lines highlight artifacts indicated by arrows of the same color. Group i shows the successful elimination of all the artifacts by the second iteration, whereas group ii shows the successful elimination of all the artifacts by the third iteration. Group iii shows the persistence of artifacts in all the iterations and the successful elimination of a false positive (iii, c.). The code for the proposed algorithm is available in the Supporting Information.

sensitive high-throughput systems for use in drug-development assays, disease modeling, and safety pharmacology.

METHODOLOGY

A detailed rendering of the complete system is shown in Figure 1A, accompanied by a close-up rendering of the core components of the system in Figure 1B,C. The principle is illustrated in Figure 1D,E. Briefly, a layer of PDMS is placed in the bottom of each well of a 96-well plate, and a dog-bone-shaped microwell is stamped into the PDMS using an inexpensive 3D printed stamp, effectively reducing the volume for growing a tissue to 20 μL. The cells are seeded into these microwells in a collagen hydrogel at concentrations ranging from 20,000 to 100,000 cells per microtissue. Once seeded, the plate is fitted with a 3D-printed rack, providing two optical microprobes per well, as shown in detail in Figure 1B-D. As the 3D microtissues form, they wrap around the flexible optical fiber segments, bringing the fibers closer to each other, as shown in Figure 1D. The initial and final distance between the two optical fiber microprobes can be tracked by imaging the bottom of the plate from a long distance (20−30 cm) using a digital single-lens reflex (DSLR) camera. Finally, a custom software processes the image of the entire plate and outputs the distance between the bright segments of the optical fibers at the initial and final timepoints, distributed by a well position. The overall microprobe displacement (δ) is then converted into microtissue contraction force according to the end-loaded cantilever-beam theory shown in Figure 1E. Details on the device fabrication process (Figure S1), including stereolithography (STL format) files and the source code for the proposed computer vision algorithm, as well as the cell culture methodology are available in the SI.

IMAGING

For imaging using standard microscopy, individual wells were imaged at 4× magnification using a light microscope (Echo Revolve, San Diego, USA) equipped with a touch-sensitive display screen and a stylus for hand annotation. Microprobe displacement was manually annotated from center to center in each image as well as subsequently measured using low-level computer vision techniques.

For the imaging of all the wells simultaneously using a digital camera, the 96-well plate was placed into a custom-designed and 3D-printed (Lulzbot Mini 2, North Dakota, USA) plate holder securely attached to the camera stand (A4 copy stand, LPL Corporation, Saitama, Japan) at a fixed position (Figure 1A). The 96-well plate was covered with a custom-designed and 3D-printed flexible plate cover (Lulzbot Mini 2, Black Ninjaflex Filament, North Dakota, USA) fitted with a custom-designed and 3D-printed slit mask (Anycubic Photon 3D Printer & Resin, Black, Shenzhen, China) aligned with wells B-G (4−9). The slit mask was important to minimize stray light scatter off the sides of the microtiter wells. Finally, an electroluminescent light panel (LightWorks Labs, New York, USA) was placed atop the cover plate and slit mask to provide uniform illumination across all the optical fiber microprobes. The entire setup was placed in a light-tight box built in-house and the microtissues imaged at distances of 20, 25, and 30 cm using a DSLR Camera (Canon Eos Rebel T7, Tokyo, Japan) equipped with a wide-angle lens (HD DSLR Macro Portion Auto Focus 0.43×, Canon, Tokyo, Japan) bolted to the camera stand, as shown in Figure 1A. Each condition was imaged with the box open to enable the image capture of the calibration grid for scale setting, followed by imaging in complete darkness to enable the image capture of light emitted from optical microprobes. The microprobe displacement was manually annotated from center to center in each well of the camera images using ImageJ (U. S. National Institutes of Health, Bethesda, Maryland, USA) and later measured via custom computer vision framework.

Object Detection and Automated Distance Quantification. For comparison purposes, the images acquired via microscopy were also tested on the custom fiber detection and distance-tracking software. The number of microns per pixel was

https://dx.doi.org/10.1021/acssensors.0c02172
ACS Sens. 2021, 6, 985−994

determined through the microscope's internal annotation software and verified through ImageJ using the average fiber diameter of hand-annotated images ($n = 10$ technical replicates), with each fiber measuring 250 μm in diameter as per the manufacturer's specifications. Images were analyzed with Python, OpenCV, and SciPy[40,41] at the original resolution to explore the relationship between the pixel size and the minimum detectable movement. After converting to 8-bit grayscale, the images were cropped to the size of the dog-bone-shaped well to reduce the processing requirements. The images were then denoised with a Gaussian blur, and a binary mask was generated using adaptive thresholding. Minimal erosion and dilation steps were then applied to further denoise the mask.

Objects present in the mask were grouped and labeled by performing connected component analysis. Objects not within ± 10% of the expected area were discarded. Tightest fit rotated bounding boxes were placed around the remaining objects in the mask. The aspect ratio of the respective bounding boxes was calculated, and any object with an aspect ratio greater than 1.2 was discarded. The remaining objects in the mask were identified as fibers. The original images were then labeled with the bounding boxes around the fibers, and the distance was determined as the Euclidian distance between the centroids of the bounding boxes. Distances were converted from pixels to micrometers with the scale determined through ImageJ. Wells with only one labeled object, objects with the angles of elevation and depression greater than 45°, and wells with unreasonable calculated distances were rejected as errors.

A similar process was followed for the full-plate images with a few additional preprocessing steps. First, the calibration grid was isolated, and the images were corrected for extrinsic parameters x, y, z rotation. Pixel to metric (μm) conversions were determined by the known value of the dimensions of the calibration grid. The image of all the wells was then divided into equal smaller images and given a label based on the well position. Individual well images were then processed in a manner similar to the one used for the microscopy images documented above. Through a series of batch image processing involving image segmentation and grayscale thresholding, as shown in Figure 2G, 1−4 the algorithm automatically detected the center of the optical fibers (highlighted in green) in each well and provided the output of the distance between the two fibers (μm) into a CSV file.

RESULTS AND DISCUSSION

The objective of this study was to develop a fast and automated method for the batch quantification of microtissue contractility in vitro. The hypothesis was that flexible optical fiber microprobes embedded in microtissues would transmit sufficient light to enable precise whole plate image quantification using a camera instead of the conventional, time-consuming, well-by-well imaging using a microscope. To verify this hypothesis, microtissues consisting of 20,000−100,000 cells per well were grown in the platform and imaged using a digital camera. To assess the impact of the focal length and pixel size on the minimum detectable movement, the images were obtained at three different focal distances (20, 25, and 30 cm). A custom-designed image-processing framework was then used to detect the optical fiber microprobes, measure the distance between the microprobes paired by well, and convert that distance from pixels to millimeters.

For validation purposes, the microscopy images of each well were also obtained at 4× magnification and optical fiber microprobe deflection measured by manually annotating the center-to-center distance between the microprobes. The manual annotation of microscopy images is the current industry standard available in most laboratories and was therefore adopted as the ground truth method for validating the automated analysis.

For comparison, contraction was also measured via the manual annotation of camera images obtained at a focal length of 20 cm using ImageJ. Microtissue contraction was evaluated across all the cellular concentrations over a period of 48 h. The accuracy of the contractility measurements obtained through all the imaging and detection methods was compared using Pearson's correlation. In addition, a comprehensive discussion of the factors influencing the accuracy of the measurements is also presented. Lastly, further microtissue contraction, as a response to the transforming growth factor beta 1 (TGF-β1) cytokine, was also evaluated.

Microprobe Tracking. Because microscopy and manual analysis are the conventional methods of measuring tissue contraction, we used such measurements to benchmark our data. The distance between the optical fiber microprobes was hand-annotated from center to center in each well using the microscope's software and a hand-held stylus. The microscope software automatically assigned a calibrated measurement value to each hand annotation based on the magnification settings (Figure 2A,B).

Similar to the full well plate images, we applied the image-processing pipeline to the microscopy images to compare manual annotation and automated fiber detection. One output of analysis was the annotated images shown in Figure 2C,D, as well as a numerical table for all wells exported as a CSV file. Microtissue contraction measurements obtained using the algorithmic analysis of the microscopy images differed by approximately ± 0.7% from the manual annotation measurements. The computer vision pipeline was able to detect fibers and reliably analyze data in 86% of the wells captured via microscopy imaging. Object detection was not possible in some of the remaining wells because of the presence of artifacts such as microprobe-sized bubbles near the periphery of the optical fibers. The ability to eliminate wells, including culture artifacts, was considered highly desirable to avoid misleading results.

Figure 2G shows the iterative process to eliminate artifacts in three different groups (i-iii). Yellow arrows point to artifacts—most commonly air bubbles—highlighted in the same color and their disappearance or persistence after successive image-processing steps (Figure 2G 2−4). Group (i) shows the successful elimination of the majority of artifacts by Gaussian blur and adaptive thresholding (Figure 2G 3), whereas Group (ii) shows the successful elimination of all the artifacts by the connected component analysis (Figure 2G 4). Group (iii) shows the persistence of artifacts after object detection and the elimination of a false positive (Figure 2Giii c.).

Finally, in order to complete the analyses of the quantitation methods, camera images taken at 20 cm were uploaded onto ImageJ − an example is shown in Figure 2E,F. The edge of the black squares in the checkerboard calibration grid was used to set the scale (3 mm) for each image and the center-to-center distance between the fibers in each well hand-annotated using the mouse cursor at the highest zoom setting within the measurement menu of the software. Numerical measurement values were output into a table within ImageJ and exported as a CSV file. Quantifying the microprobe displacement using ImageJ proved to be the most challenging quantitation method.

https://dx.doi.org/10.1021/acssensors.0c02172
ACS Sens. 2021, 6, 985−994

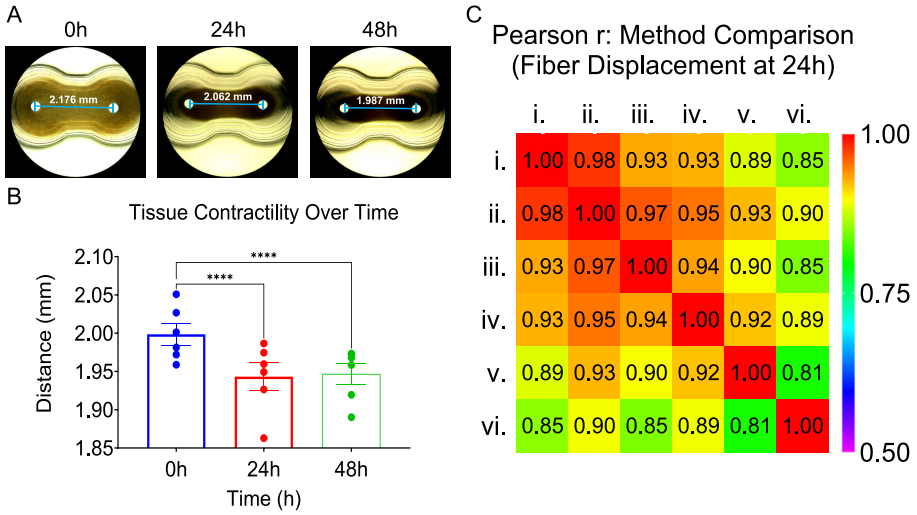

Figure 3. Effectiveness of the proposed method and how the different image capture methods compare. (A) Time-lapse microscopy images (4× magnification) obtained for a tissue containing 60,000 cells showing the hand-annotated distances between the fibers for d_{0h} = 2.176 mm, d_{24h} = 2.062 mm, d_{48h} = 1.987 mm. (B) Graph showing significant tissue contraction for all the cell concentrations after 24 and 48 h (mean ± SEM, two-way analysis of variance, 95% confidence level, ****$p < 0.0001$, $n = 6$ microtissues per condition produced in a single experiment), (C) Pearson r correlation graph showing how the camera image algorithmic detection method for images taken at 20 cm (iii), 25 cm (iv), and 30 cm (v) correlate strongly with the standard method of manual annotation of microscopy images (i) ($0.89 < r < 0.93$), as well as the microscopy image algorithmic detection method (ii) ($r = 0.98$), with the ImageJ hand-annotation method (vi) showing the weakest correlation ($r = 0.85$) (Pearson r correlation, 95% confidence interval, n = 36 microtissues produced in a single experiment). See SI Figure S6 for the correlation plots for each method.

Unlike the microscopy images in which physical magnification is attained with the use of powerful lenses, the annotation of camera images on ImageJ relies on the zoom associated with each image. Therefore, as the physical size of the probe is smaller in the camera image, the accuracy in determining the center of the microprobe is reduced.

Microprobe Contrast. Image-processing software is commonly equipped with brightness- and contrast-adjustment options. Brightness adjustment involves changing the pixel intensity values of the red, green, and blue channels that compose the image, whereas contrast adjustments involve reassigning pixel values toward black or white channels, depending on how they compare to a specific value. Although brightness and contrast adjustments can be applied to an entire image, these adjustment tools do not correct for the intrinsic luminance of specific features unless these have been purposefully marked or identified. Micropillar-based contractility studies rely on the ability to optically distinguish micropillars from artifacts, bubbles, or microtissues. Conventional PDMS micropillars do not offer high luminance, as they are not efficient light guides. As a result, the PDMS micropillar-based contractility measurements rely on high-resolution microscopy imaging and expert inspection to be visually resolved.

The proposed system, on the other hand, is based on the premise that optical fiber microprobes act as efficient light guides with high luminance, allowing microprobe boundaries to be visually resolved at lower resolutions. As it can be seen in Figure 3A, the optical fiber microprobes are clearly visible during all the stages of microtissue formation, thus confirming this proposition. Further information on microprobe contrast is discussed in the Supporting Information (Figure S4). In addition to serving as bright point-source physical beacons, optical fiber microprobes offer well-defined high-contrast borders, which enable accurate centering and scale setting. In this case, the pixel intensities are well defined across the microprobe−microtissue interface, forming a defined outline as the result of the juxtaposition of highly contrasting pixels. This is particularly important when imaging the microprobes at larger focal distances. In these instances, the number of pixels across the microprobe−tissue interface is considerably reduced. As a result, micropillar border definition relies even more on the juxtaposition of highly contrasting pixels, which is made possible using this optical fiber microprobe system.

Microprobe Resolution. In the proposed study, micropillar deflection measurements correspond to the discrete pixel count between two microprobes. Therefore, the theoretical limit of detection of microprobe displacement is limited to the pixel size of each image. The pixel size is a function of image resolution and the image size. For instance, the microscopy and the camera images used in this study exhibit the same resolution (72 dpi); however, after taking into account magnification and focal distances, the microscopy images exhibit a measured experimental pixel size of 1.5 μm/pixel, whereas the camera images exhibit measured pixel sizes of 25 μm/pixel (focal distance = 20 cm), 32.6 μm/pixel (focal distance = 25 cm), and 42.85 μm/pixel (focal distance = 30 cm). By inputting these displacement values ($\delta_{\text{Single microprobe}}$ = pixel size/2) into the cantilever-beam equation shown in Figure 1, it is possible to predict the theoretical limit of detection of microtissue contractility for each imaging method: microscopy ($0.02 \pm 6.76 \times 10^{-5}$ mN), 20 cm camera images ($0.27 \pm 1.88 \times 10^{-2}$ mN), 25 cm camera images (0.35 mN $\pm 3.19 \times 10^{-2}$ mN), and 30 cm camera images (0.45 mN $\pm 5.52 \times 10^{-2}$ mN). More information on error calculation is available in the Supporting Information.

Image Distortion. One aim of the present study was to characterize the optical microprobe system in its most compact configuration. To this end, short focal distances ranging from 20−30 cm were used to image the centermost region of the 96-well plate. Imaging at short focal distances offers advantages and disadvantages. The advantages include higher image definition and an overall compact experimental setup. The disadvantages

https://dx.doi.org/10.1021/acssensors.0c02172
ACS Sens. 2021, 6, 985−994

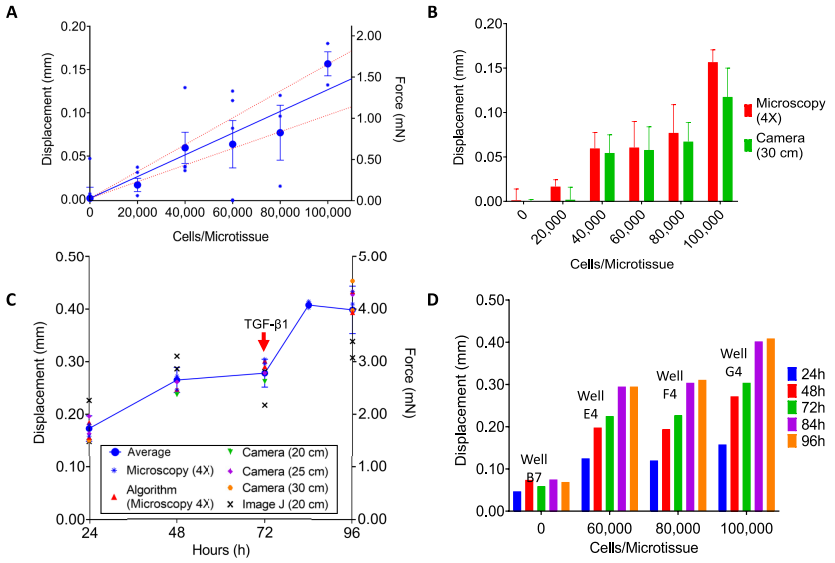

Figure 4. Effect of cell concentration and time on microtissue contraction. (A) Effect of cell concentration on the optical fiber displacement and force at 24 h (mean ± SEM, simple linear regression (blue line), 95% confidence interval (dotted red lines), $n = 6$ microtissues per condition produced in a single experiment, (*) Individual values, (●) Average values), (B) Method comparison showing the average microtissue contraction measurements for different cell concentrations obtained via microscopy and camera imaging at 24 h (mean ± SEM, two imaging methods, $n = 6$ microtissues per condition produced in a single experiment) (C) Representative time course graph showing the contraction pattern of microtissues containing 100,000 cells before and after the addition of TGF-β1 at 72 h imaged using all the imaging methods (mean ± SD, six imaging methods, $n = 2$ microtissues per condition produced in a single experiment) (D) Microscopy displacement over 96 h for different cell concentrations ranging from 0−100,000 cells before and after the addition of TGF-β1 at 72 h showing significant increase ($p = 0.009$) in contraction for microtissues containing 60,000, 80,000, and 100,000 cells at 96 h (one-way analysis of variance, Dunnett's multiple comparison test, 95% confidence interval, $n = 4$ microtissues produced in a single experiment: wells B7, E4, F4, and G4).

include the fisheye effect on the image and distortion amplification if the plate is rotated in any of its axes. Figure 2E shows the fisheye effect after wide-angle lens correction.

Rectilinear correction using a wide-angle lens is difficult to achieve at short focal distances. However, good correlation exists between ground truth and images captured at 20, 25, and 30 cm focal lengths using a wide-angle lens, even with minimal rectilinear correction, as shown in Figure 3C. Extrinsic correction parameters such as plate rotation on the x, y, and z-axes can be adjusted to correct for minor differences when placing the well plates on the plate holder for imaging. Rectilinear correction factors for intrinsic camera parameters such as lens effects at various focal lengths can be manually entered prior to image processing. Rotations on the x and y-axes are minimized by fixing the well plate aligning mount and camera-imaging plane in parallel. The ability to apply image corrections enables the use of the entire 96-well plate at larger focal distances or the segmentation of the plate into quadrants.

Other strategies to increase the accuracy include a focus sweep of the plate followed by multi-image burst acquisition. While determining centroid-to-centroid distance helps reduce errors from the poor edge detection of out-of-focus fibers, focus sweeps would help increase the percentage of in-focus images in the data set. Multi-image burst acquisition would help reduce errors from transient artifacts that cause wells to be skipped during full-plate image analysis. Furthermore, increasing the size of the image sets can improve the accuracy of the automated measurements by providing a route to applying machine-learning techniques with powerful training sets. Accordingly, video recording may be particularly useful in tissues with high-frequency movement, such as cardiac tissue constructs beating during imaging. It is important to highlight that, in all instances, whole plate imaging or quadrant imaging is orders of magnitude faster than microscopy imaging and manual annotation.

Microprobe Displacement. Figure 3A shows a time-lapse series of brightfield microscopy images obtained at 4× magnification outlining the distance between the optical fiber microprobes (round white) embedded in the microtissues (light/dark brown) as the tissues form over a period of 48 h. Figure 3A shows microtissue formation in a representative sample containing 60,000 cells dispersed in 20 μL of 6 mg mL^{-1} collagen hydrogel in a loose conformation at time zero (d_{0h} = 2.176 mm), progressing to a fusiform structure after 24 h (d_{24h} = 2.062 mm) and 48 h (d_{48h} = 1.987 mm). Figure 3B shows that significant microtissue contraction ($p < 0.0001$) is achieved for all the microtissues after a period of 24 h remaining relatively unchanged after 48 h. These results indicate that 24 h is a suitable timepoint to measure significant fusiform microtissue formation. Detailed information on microtissue variability is shown in the Supporting Information (Figure S4).

Pearson r correlation was chosen as a suitable statistical method to compare the microprobe displacement measurements obtained via different methods. Figure 3C shows the Pearson r correlation for the fiber displacement at the 24 h timepoint measured using different imaging and detection methods. The images obtained via microscopy, annotated using the manual annotation method, were representative of the current industry standard method and served as the ground truth for validating our proposed method. Figure 3C shows that in a direct well-to-well comparison (n = 36 microtissues produced in a single experiment), the accuracy of the algorithmic detection method for the camera images taken at 20 cm (Figure 3C iii), 25 cm (Figure 3C iv), and 30 cm (Figure 3C v) strongly correlated with that of the current industry standard (Figure 3C i).

https://dx.doi.org/10.1021/acssensors.0c02172
ACS Sens. 2021, 6, 985−994

Notably, the full-plate image-processing pipeline showed a strong correlation (r = 0.93) for the images taken with a DSLR camera at 20 and 25 cm and a slightly lower correlation (r = 0.89) for images taken at 30 cm. The image analysis method for the microscopy images (Figure 3C ii) showed the highest correlation (r = 0.98) with the standard method as the microscopy images exhibit a much higher resolution compared to the images obtained using a DSLR camera. Furthermore, the algorithmic detection method for the 20 cm image was superior (r = 0.93) to the manual annotation method of the 20 cm camera images using ImageJ (r = 0.85). In addition, Figure 3C vi shows how the camera image quantification method using ImageJ annotation correlates with the algorithmic detection method for the camera images taken at 20 cm (r = 0.85), 25 cm (r = 0.89), and a lowest correlation (r = 0.81) for the images taken at 30 cm. Lower correlation values obtained for ImageJ quantification can be attributed to the user error when manually annotating center-to-center distances between the microprobes in the camera images.

The data suggest that the proposed platform and analytical algorithm can be used in conjunction as a valid analytical method for the high-throughput quantification of microtissue contractility in vitro, without the need for complex machine learning or processor-intensive techniques. Moreover, the results suggest that, in the absence of computer vision object detection and automated distance analysis, camera image quantification using ImageJ is a suitable method for the quantitation of whole plate images obtained with a DSLR camera at 25 cm (r = 0.89).

Microtissue Contraction. The utility of the optical microprobe analytical system was demonstrated with microtissues formed de novo. The present study also addressed the influence of initial cell number, the ability to do extended time course studies, and the sensitivity to factors known to trigger tissue contraction.

Tissue contractility was evaluated in 20 μL microtissues initially seeded at six different cell concentrations 0, 20,000, 40,000, 60,000, 80,000, and 100,000 cells in 6 mg mL^{-1} collagen type I. Each condition was tested six times (n = 6 microtissues per condition produced in a single experiment) at 0 and 24 h. Statistical analysis showed that tissue contractility data were found to be normally distributed within each experimental condition according to both the Shapiro–Wilk test (alpha = 0.01) and the Kolmogorov–Smirnov test (alpha = 0.01). Grubbs' test (alpha = 0.2) was then applied to each experimental condition to remove outliers (Figure 4A,B). It is important to highlight that the cells used in this experiment were derived from a primary cell line with a doubling rate of approximately 36 h. Hence, microtissue contraction at the 24 h timepoint was deemed to be a representative measure of the traction generated by the initial cell concentration.

As shown in Figure 4A, microtissue contractility is a direct function of cellular concentration. Under these conditions, the entire 20 μL volume visibly contracted in all the directions and formed a fusiform structure around the optical fiber microprobes in each well.

Figure 4A shows microtissue contraction in millimeters (mm) and microtissue force in millinewtons (mN) on the same graph. Microtissue forces were calculated based on the end-loaded cantilever-beam deflection theory described in Figure 1E. The elastic modulus of the optical fibers was measured experimentally (Instron, Norwood, MA, USA) and was found to be 1.975 GPa. The free-moving length L of the optical fiber micropillars was 9.5 mm, and the optical fiber diameter was 250 μm. Microtissue forces ranging from 0.17–1.7 mN were obtained for tissues containing 20,000–100,000 cells. Figure 4B documents that this initial contraction is evident whether the microtissue displacements are measured on a well-by-well basis using microscopy or across all the wells simultaneously using photography.

Figure 4C shows that the proposed system is sensitive enough to measure microtissue deformation upon the addition of a cytokine (10 ng/mL TGF-β1) at 72 h (six imaging methods, n = 2 microtissues per condition produced in a single experiment). More information on additional induced contractility assays using homotypic and heterotypic microtissues is available in the Supporting Information (Figure S3). Figure 4D shows that the microtissues across a variety of cell concentrations are still viable and responsive after 96 h. The fluorescent microscopy images of the cell viability assay at the 96-h endpoint are provided in the Supporting Information (Figure S5).

FUTURE APPLICATIONS

The sensitivity of the proposed platform, together with the ability to maintain cell viability over long periods of time, may therefore enable the study of cellular responses in real time, such as cardiomyocyte contraction,[1,5,34,35,42,43] or changes over time, such as fibroblast contraction as a response to activation toward a myofibroblast phenotype, as previously described.[24,44]

Advances in tissue engineering have enabled researchers to evaluate tissue contractility in homotypic and heterotypic microtissues.[45] One example of a well-studied heterotypic microtissue is the engineered heart tissue (EHT) in which cardiomyocytes, resident macrophages, cardiac microvascular endothelial cells, and cardiac fibroblasts can be combined to model human cardiac tissue in vitro.[2,5,17,32,34,46–49] Tissue contraction measurements are key to evaluate EHT contractility, structure, and function, as well as specific cellular responses to physicochemical stimulation.[2,5,17,32,46–48,50–55] More specifically, the models of human cardiac tissue are highly desirable to recapitulate human physiology as certain ion channels, including the human ether-a-go-go (hERG) and KvLQT1 potassium channels, cannot be tested in vivo.[2,56] In 2005, this fundamental limitation led the International Council for the Harmonization of Technical Requirements for Pharmaceuticals for Human Use to call for the development of microphysiological platforms for EHT testing in vitro[56] through the comprehensive in vitro proarrhythmia assay initiative.[57] Since then, microphysiological platforms have become the new paradigm for cardiac disease modeling, drug development, and safety pharmacology studies in vitro.[4–6] In this context, the proposed system can be scaled to fit other microtiter plate sizes and incorporate additional characterization tools, such as electrodes for sensing or stimulation.

Furthermore, the computer vision algorithm herein presented can analyze the video captured using a high-speed camera enabling continuous frame-based video readouts for whole-plate quantification. Further information on how image resolution, focal distance, and acquisition rate influence analytical sensitivity is presented in the Supporting Information (Table S3 and Figure S2).

Moreover, as all living mammalian cells exert traction forces via adhesion to either the extracellular matrix (ECM) or to the neighboring cells, tissue contraction measurements can also be used to evaluate tissue contractility, structure, and function.[58] Furthermore, as the contractile properties of cells can change

https://dx.doi.org/10.1021/acssensors.0c02172
ACS Sens. 2021, 6, 985–994

with variations in cell−ECM interactions, tissue contraction measurements can also help evaluate the mechanical compliance of artificial ECM substrates and their ability to support natural tissue functions.[58,59]

Finally, based on the capabilities of the system demonstrated here, emerging research areas that could benefit from the proposed method include tissue morphogenesis;[58,60,61] tumor progression;[62] regeneration of skeletal, cardiac, and smooth muscles;[10,63] and wound healing.[16,26,64−67]

CONCLUSIONS

A novel and inexpensive tissue engineering platform provides for the high-throughput quantification of microtissue contractility in a 96-well plate configuration. The platform integrates 3D printed parts fitted with flexible optical fiber microprobes embedded in contractile microtissues for batch quantification via camera imaging and low-power algorithmic quantitation of tissue contraction. This is the first platform of its kind based on the principle that optical fiber microprobes can serve as bright beacons for microtissue quantification using the cantilever-beam theory. The study shows that the computer vision preprocessing, object detection, and distance analysis techniques, allied with the precision with which the movement of the optical fiber microprobes can be detected, enables accurate contractility measurements, which would otherwise not be achieved with the use of camera images. The proposed algorithm can accurately determine microprobe centroids, eliminate artifacts, and correct for extrinsic and intrinsic camera parameters, thus enabling precise pixel-based quantification even in images in which the diameter of the microprobes is an order of magnitude smaller than that in the standard methods for imaging and quantification. This high-throughput platform strategy offers an inexpensive and scalable concept that is sufficiently sensitive to quantify microtissue contraction in batch systems. Finally, it is proposed that this platform may be useful for microtissue engineering, disease modeling, drug development, and safety pharmacology.

ASSOCIATED CONTENT

Supporting Information

The Supporting Information is available free of charge at https://pubs.acs.org/doi/10.1021/acssensors.0c02172.

> Information on analogous systems, device fabrication and cell culture methods, STL files for the 3D-printed parts shown in Figure 1, computer vision algorithm, error calculations, detection of fast-moving tissues, induced contractility assays, microtissue variability, fluorescence microscopy images of the cell viability assay at the 96 h timepoint, and Pearson's correlation plots for the data presented in Figure 3C (PDF)

AUTHOR INFORMATION

Corresponding Author

Donald O. Freytes − *Joint Department of Biomedical Engineering, University of North Carolina-Chapel Hill/North Carolina State University, Raleigh 27695, North Carolina, United States; Comparative Medicine Institute, North Carolina State University, Raleigh 27695, North Carolina, United States*; Email: dofreyte@ncsu.edu

Authors

Ana Maria Gracioso Martins − *Joint Department of Biomedical Engineering, University of North Carolina-Chapel Hill/North Carolina State University, Raleigh 27695, North Carolina, United States; Comparative Medicine Institute, North Carolina State University, Raleigh 27695, North Carolina, United States*; orcid.org/0000-0001-7633-6676

Michael D. Wilkins − *Comparative Medicine Institute and Department of Electrical and Computer Engineering, North Carolina State University, Raleigh 27695, North Carolina, United States*

Frances S. Ligler − *Joint Department of Biomedical Engineering, University of North Carolina-Chapel Hill/North Carolina State University, Raleigh 27695, North Carolina, United States; Comparative Medicine Institute, North Carolina State University, Raleigh 27695, North Carolina, United States*; orcid.org/0000-0003-4909-2084

Michael A. Daniele − *Joint Department of Biomedical Engineering, University of North Carolina-Chapel Hill/North Carolina State University, Raleigh 27695, North Carolina, United States; Comparative Medicine Institute and Department of Electrical and Computer Engineering, North Carolina State University, Raleigh 27695, North Carolina, United States*; orcid.org/0000-0002-2016-4091

Complete contact information is available at: https://pubs.acs.org/10.1021/acssensors.0c02172

Author Contributions

The manuscript was written through contributions of all authors. All authors have given approval to the final version of the manuscript.

Funding

Funding was provided by North Carolina State University, by the Ross M. Lampe Chair in Biomedical Engineering. M.D. was supported by the National Science Foundation (CCSS-1846911). D.O.F. was partially funded by the National Institutes of Health/National Institute on Deafness and Other Communication Disorders (R01DC017139, R01DC017743).

Notes

The authors declare no competing financial interest.

ACKNOWLEDGMENTS

We thank the North Carolina State University Comparative Medicine Institute for supporting interdisciplinary research. The authors would like to thank Dr. Qingshan Wei for helping with the experimental imaging setup, as well as undergraduate students Isabel Mayo, Genevieve P. Morrissey, Melodie J. Chang, and Drew DiSerafino for their assistance. The graphical abstract was created using BioRender.com.

REFERENCES

(1) Vandenburgh, H.; Shansky, J.; Benesch-Lee, F.; Barbata, V.; Reid, J.; Thorrez, L.; Valentini, R.; Crawford, G. Drug-Screening Platform Based on the Contractility of Tissue-Engineered Muscle. *Muscle & Nerve* **2008**, *37*, 438−447.

(2) Hirt, M. N.; Hansen, A.; Eschenhagen, T. Cardiac Tissue Engineering: State of the Art. *Circ. Res.* **2014**, *114*, 354−367.

(3) Anonymous. Safety Pharmacology Studies for Human Pharmaceuticals S7A; International Conference on Harmonisation of Technical Requirements for Registration of Pharmaceuticals for Human Use, Ed.; International Conference on Harmonisation of Technical Requirements for Registration of Pharmaceuticals for

Human Use: https://database.ich.org/sites/default/files/S7A_Guideline.pdf , 2000.
(4) Ogle, B. M.; Bursac, N.; Domian, I.; Huang, N. F.; Menasché, P.; Murry, C. E.; Pruitt, B.; Radisic, M.; Wu, J. C.; Wu, S. M.; et al. Distilling Complexity to Advance Cardiac Tissue Engineering. *Sci. Transl. Med.* **2016**, *8*, 342ps13−342ps13.
(5) Mannhardt, I.; Saleem, U.; Benzin, A.; Schulze, T.; Klampe, B.; Eschenhagen, T.; Hansen, A. Automated Contraction Analysis of Human Engineered Heart Tissue for Cardiac Drug Safety Screening. *J. Visual. Exp: JoVE* **2017**, *e55461*, 1−10.
(6) Watson, D. E.; Hunziker, R.; Wikswo, J. P. Fitting Tissue Chips and Microphysiological Systems into the Grand Scheme of Medicine, Biology, Pharmacology, and Toxicology. *Exp. Biol. Med.* **2017**, *242*, 1559−1572.
(7) Kolodney, M. S.; Wysolmerski, R. B. Isometric Contraction by Fibroblasts and Endothelial Cells in Tissue Culture: A Quantitative Study. *J. Cell Biology* **1992**, *117*, 73−82.
(8) Polacheck, W. J.; Chen, C. S. Measuring Cell-Generated Forces: A Guide to the Available Tools. *Nat. Methods* **2016**, *13*, 415−423.
(9) Walker, M.; Rizzuto, P.; Godin, M.; Pelling, A. E. Structural and Mechanical Remodeling of the Cytoskeleton Maintains Tensional Homeostasis in 3D Microtissues under Acute Dynamic Stretch. *Sci. Rep.* **2020**, *10*, 1−16.
(10) Elliott, N. T.; Yuan, F. A Review of Three-Dimensional in Vitro Tissue Models for Drug Discovery and Transport Studies. *J. Pharm. Sci.* **2011**, *100*, 59−74.
(11) Kang, H.-W.; Lee, S. J.; Ko, I. K.; Kengla, C.; Yoo, J. J.; Atala, A. A 3D Bioprinting System to Produce Human-Scale Tissue Constructs with Structural Integrity. *Nat. Biotechnol.* **2016**, *34*, 312−319.
(12) Sakar, M. S.; Neal, D.; Boudou, T.; Borochin, M. A.; Li, Y.; Weiss, R.; Kamm, R. D.; Chen, C. S.; Asada, H. H. Formation and Optogenetic Control of Engineered 3D Skeletal Muscle Bioactuators. *Lab Chip* **2012**, *12*, 4976−4985.
(13) Kimlin, L.; Kassis, J.; Virador, V. 3D in Vitro Tissue Models and Their Potential for Drug Screening. *Expert Opin Drug Discov* **2013**, *8*, 1455−1466.
(14) Grill, S. W. Growing up Is Stressful: Biophysical Laws of Morphogenesis. *Curr. Opin. Genet. Dev.* **2011**, *21*, 647−652.
(15) Fabre, K. M.; Livingston, C.; Tagle, D. A. Organs-on-Chips (microphysiological Systems): Tools to Expedite Efficacy and Toxicity Testing in Human Tissue. *Exp. Biol. Med. (Maywood)* **2014**, *239*, 1073−1077.
(16) Auger, F. A.; Berthod, F.; Moulin, V.; Pouliot, R.; Germain, L. Tissue-Engineered Skin Substitutes: From in Vitro Constructs to in Vivo Applications. *Biotechnol. Appl. Biochem.* **2004**, *39*, 263−275.
(17) Zimmermann, W.-H.; Schneiderbanger, K.; Schubert, P.; Didie, M.; Munzel, F.; Heubach, J.; Kostin, S.; Neuhuber, W.; Eschenhagen, T. Tissue Engineering of a Differentiated Cardiac Muscle Construct. *Circ. Res.* **2002**, *90*, 223−230.
(18) Pampaloni, F.; Stelzer, E. H.; Masotti, A. ThreeDimensional Tissue Models for Drug Discovery and Toxicology. *Recent Pat. Biotechnol.* **2009**, *3*, 103−117.
(19) Marquez, J. P.; Legant, W.; Lam, V.; Cayemberg, A.; Elson, E.; Wakatsuki, T. High-Throughput Measurements of Hydrogel Tissue Construct Mechanics. *Tis. Engineer. Part C: Methods* **2009**, *15*, 181−190.
(20) Legant, W. R.; Pathak, A.; Yang, M. T.; Deshpande, V. S.; McMeeking, R. M.; Chen, C. S. Microfabricated Tissue Gauges to Measure and Manipulate Forces from 3D Microtissues. *Proc.Nat. Acad. of Sci.* **2009**, *106*, 10097−10102.
(21) Wells, R. G. Tissue Mechanics and Fibrosis. *Biochimica et Biophysica Acta (BBA) − Mol. Basis of Disease* **2013**, *1832*, 884−890.
(22) Afshar, M. E.; Abraha, H. Y.; Bakooshli, M. A.; Davoudi, S.; Thavandiran, N.; Tung, K.; Ahn, H.; Ginsberg, H. J.; Zandstra, P. W.; Gilbert, P. M. A 96-Well Culture Platform Enables Longitudinal Analyses of Engineered Human Skeletal Muscle Microtissue Strength. *Sci. Rep.* **2020**, *10*, 1−16.
(23) West, A. R.; Zaman, N.; Cole, D. J.; Walker, M. J.; Legant, W. R.; Boudou, T.; Chen, C. S.; Favreau, J. T.; Gaudette, G. R.; Cowley, E. A.; et al. Development and Characterization of a 3D Multicell Microtissue Culture Model of Airway Smooth Muscle. American Journal of Physiology-Lung Cellular and Molecular. *Physiology* **2013**, *304*, L4−L16.
(24) Asmani, M.; Velumani, S.; Li, Y.; Wawrzyniak, N.; Hsia, I.; Chen, Z.; Hinz, B.; Zhao, R. Fibrotic Microtissue Array to Predict Anti-Fibrosis Drug Efficacy. *Nat. Commun.* **2018**, *9*, 2066−2078.
(25) Chen, Z.; Wang, Q.; Asmani, M.; Li, Y.; Liu, C.; Li, C.; Lippmann, J. M.; Wu, Y.; Zhao, R. Lung Microtissue Array to Screen the Fibrogenic Potential of Carbon Nanotubes. *Sci. Rep.* **2016**, *6*, 31304−31314.
(26) Sakar, M. S.; Eyckmans, J.; Pieters, R.; Eberli, D.; Nelson, B. J.; Chen, C. S. Cellular Forces and Matrix Assembly Coordinate Fibrous Tissue Repair. *Nat. Commun.* **2016**, *7*, 11036−11044.
(27) Van Spreeuwel, A. C. C.; Bax, N. A. M.; Bastiaens, A. J.; Foolen, J.; Loerakker, S.; Borochin, M.; van der Schaft, D. W. J.; Chen, C. S.; Baaijens, F. P. T.; Bouten, C. V. C. The Influence of Matrix (an)isotropy on Cardiomyocyte Contraction in Engineered Cardiac Microtissues. *Integr Biol (Camb)* **2014**, *6*, 422−429.
(28) Hansen, A.; Eder, A.; Bönstrup, M.; Flato, M.; Mewe, M.; Schaaf, S.; Aksehirlioglu, B.; Schwörer, A.; Uebeler, J.; Eschenhagen, T. Development of a Drug Screening Platform Based on Engineered Heart Tissue. *Circ. Res.* **2010**, *107*, 35−44.
(29) Chen, Z.; Lu, J.; Zhang, C.; Hsia, I.; Yu, X.; Marecki, L.; Marecki, E.; Asmani, M.; Jain, S.; Neelamegham, S.; et al. Microclot Array Elastometry for Integrated Measurement of Thrombus Formation and Clot Biomechanics under Fluid Shear. *Nat. Commun.* **2019**, *10*, 2051−2063.
(30) Wang, H.; Svoronos, A. A.; Boudou, T.; Sakar, M. S.; Schell, J. Y.; Morgan, J. R.; Chen, C. S.; Shenoy, V. B. Necking and Failure of Constrained 3D Microtissues Induced by Cellular Tension. *Proc.Nat. Acad. of Sci.* **2013**, *110*, 20923−20928.
(31) Trichet, L.; Le Digabel, J.; Hawkins, R. J.; Vedula, S. R. K.; Gupta, M.; Ribrault, C.; Hersen, P.; Voituriez, R.; Ladoux, B. Evidence of a Large-Scale Mechanosensing Mechanism for Cellular Adaptation to Substrate Stiffness. *Proc.Nat. Acad. of Sci.* **2012**, *109*, 6933−6938.
(32) Mannhardt, I.; Breckwoldt, K.; Letuffe-Brenière, D.; Schaaf, S.; Schulz, H.; Neuber, C.; Benzin, A.; Werner, T.; Eder, A.; Schulze, T.; et al. Human Engineered Heart Tissue: Analysis of Contractile Force. *Stem Cell Rep.* **2016**, *7*, 29−42.
(33) Zhao, R.; Boudou, T.; Wang, W.-G.; Chen, C. S.; Reich, D. H. Decoupling Cell and Matrix Mechanics in Engineered Microtissues Using Magnetically Actuated Microcantilevers. *Adv. Mater. Weinheim* **2013**, *25*, 1699−1705.
(34) Ronaldson-Bouchard, K.; Ma, S. P.; Yeager, K.; Chen, T.; Song, L.; Sirabella, D.; Morikawa, K.; Teles, D.; Yazawa, M.; Vunjak-Novakovic, G. Advanced Maturation of Human ardiac Tissue Grown from Pluripotent Stem Cells. *Nature* **2018**, *556*, 239−243.
(35) Bielawski, K. S.; Leonard, A.; Bhandari, S.; Murry, C. E.; Sniadecki, N. J. Real-Time Force and Frequency Analysis of Engineered Human Heart Tissue Derived from Induced Pluripotent Stem Cells Using Magnetic Sensing. *Tiss. Engineer. Part C: Methods* **2016**, *22*, 932−940.
(36) Zhao, Y.; Wang, E. Y.; Davenport, L. H.; Liao, Y.; Yeager, K.; Vunjak-Novakovic, G.; Radisic, M.; Zhang, B. A Multimaterial Microphysiological Platform Enabled by Rapid Casting of Elastic Microwires. *Adv. Healthcare Mater.* **2019**, *8*, 1801187−1801196.
(37) Zhong, B.; Pan, S.; Wang, C.; Wang, T.; Du, J.; Chen, D.; Cao, L. Robust Individual-Cell/Object Tracking via PCANet Deep Network in Biomedicine and Computer Vision. *BioMed. Res. Inter.* **2016**, *2016*, 1−7.
(38) Jerbić, B.; Šuligoj, F.; Švaco, M.; Šekoranja, B. Robot Assisted 3D Point Cloud Object Registration. *Procedia Engineer.* **2015**, *100*, 847−852.
(39) Peng, H. Bioimage Informatics: A New Area of Engineering Biology. *Bioinformatics* **2008**, *24*, 1827−1836.
(40) Bradski, G.; Kaehler, A. *OpenCV Dr. Dobb's Journal of Software Tools*; 2000, *3*, 1−81.

https://dx.doi.org/10.1021/acssensors.0c02172
ACS Sens. 2021, 6, 985−994

(41) Virtanen, P.; Gommers, R.; Oliphant, T. E.; Haberland, M.; Reddy, T.; Cournapeau, D.; Burovski, E.; Peterson, P.; Weckesser, W.; Bright, J.; et al. SciPy 1.0: Fundamental Algorithms for Scientific Computing in Python. *Nat. Methods* **2020**, *17*, 261−272.
(42) Marsano, A.; Conficconi, C.; Lemme, M.; Occhetta, P.; Gaudiello, E.; Votta, E.; Cerino, G.; Redaelli, A.; Rasponi, M. Beating Heart on a Chip: A Novel Microfluidic Platform to Generate Functional 3D Cardiac Microtissues. *Lab Chip* **2016**, *16*, 599−610.
(43) Serrao, G. W.; Turnbull, I. C.; Ancukiewicz, D.; Kim, D. E.; Kao, E.; Cashman, T. J.; Hadri, L.; Hajjar, R. J.; Costa, K. D. MyocyteDepleted Engineered Cardiac Tissues Support Therapeutic Potential of Mesenchymal Stem Cells. *Tissue Eng Part A* **2012**, *18*, 1322−1333.
(44) Van den Borne, S. W. M.; Diez, J.; Blankesteijn, W. M.; Verjans, J.; Hofstra, L.; Narula, J. Myocardial Remodeling after Infarction: The Role of Myofibroblasts. *Nat Rev Cardiol* **2010**, *7*, 30−37.
(45) Youssef, J.; Chen, P.; Shenoy, V. B.; Morgan, J. R.; Mechanotransduction, I. Enhanced by the Synergistic Action of Heterotypic Cell Interactions and TGF-β1. *The FASEB Journal* **2012**, *26*, 2522−2530.
(46) Iyer, R. K.; Chiu, L. L.; Reis, L. A.; Radisic, M. Engineered Cardiac Tissues. *Curr. Opin. Biotechnol.* **2011**, *22*, 706−714.
(47) Veldhuizen, J.; Migrino, R. Q.; Nikkhah, M. ThreeDimensional Microengineered Models of Human Cardiac Diseases. *J. Biol. Engineer.* **2019**, *13*, 1−12.
(48) Ravenscroft, S. M.; Pointon, A.; Williams, A. W.; Cross, M. J.; Sidaway, J. E. Cardiac Non-Myocyte Cells Show Enhanced Pharmacological Function Suggestive of Contractile Maturity in Stem Cell Derived Cardiomyocyte Microtissues. *Toxicol. Sci.* **2016**, *152*, 99−112.
(49) Ronaldson-Bouchard, K.; Vunjak-Novakovic, G. Organson-a-Chip: A Fast Track for Engineered Human Tissues in Drug Development. *Cell Stem Cell* **2018**, *22*, 310−324.
(50) Tandon, N.; Cannizzaro, C.; Chao, P.-H. G.; Maidhof, R.; Marsano, A.; Au, H. T. H.; Radisic, M.; Vunjak-Novakovic, G. Electrical Stimulation Systems for Cardiac Tissue Engineering. *Nat. Protoc.* **2009**, *4*, 155−173.
(51) Tandon, N.; Marsano, A.; Maidhof, R.; Wan, L.; Park, H.; Vunjak-Novakovic, G. Optimization of Electrical Stimulation Parameters for Cardiac Tissue Engineering. *J. Tissue Engineer. and Regener. Med* **2011**, *5*, e115−e125.
(52) Tandon, N.; Marsano, A.; Maidhof, R.; Numata, K.; Montouri-Sorrentino, C.; Cannizzaro, C.; Voldman, J.; Vunjak-Novakovic, G. Surface-Patterned Electrode Bioreactor for Electrical Stimulation. *Lab Chip* **2010**, *10*, 692−700.
(53) Tandon, N.; Taubman, A.; Cimetta, E.; Saccenti, L.; Vunjak-Novakovic, G. Portable Bioreactor for Perfusion and Electrical Stimulation of Engineered Cardiac Tissue. *In Engineering in Medicine and Biology Society (EMBC), 35th Annual International Conference of the IEEE*; 2013; 6219−6223.
(54) Maidhof, R.; Tandon, N.; Lee, E. J.; Luo, J.; Duan, Y.; Yeager, K.; Konofagou, E.; Vunjak-Novakovic, G. Biomimetic Perfusion and Electrical Stimulation Applied in Concert Improved the Assembly of Engineered Cardiac Tissue. *J. Tissue Engineer. and Regener. Med.* **2012**, *6*, e12−e23.
(55) Zhao, Y.; Rafatian, N.; Wang, E. Y.; Feric, N. T.; Lai, B. F.; Knee-Walden, E. J.; Backx, P. H.; Radisic, M. Engineering Microenvironment for Human Cardiac Tissue Assembly in Heart-on-aChip Platform. *Matrix Biol.* **2020**, *85*, 189−204.
(56) Anonymous. International Conference on Harmonisation Guidance on S7B Non-Clinical Evaluation of the Potential for Delayed Ventricular Repolarization (QT Interval Prolongation) by Human Pharmaceuticals; International Conference on Harmonisation of Technical Requirements for Registration of Pharmaceuticals for Human Use, Ed.; International Conference on Harmonisation of Technical Requirements for Registration of Pharmaceuticals for Human Use: https://database.ich.org/sites/default/files/S7B_Guideline.pdf , 2005.
(57) Colatsky, T.; Fermini, B.; Gintant, G.; Pierson, J. B.; Sager, P.; Sekino, Y.; Strauss, D. G.; Stockbridge, N. The Comprehensive in Vitro Proarrhythmia Assay (CiPA) Initiative—update on Progress. *J. Pharmacol. Toxicol. Methods* **2016**, *81*, 15−20.
(58) Ingber, D. E. Tensegrity-Based Mechanosensing from Macro to Micro. *Prog. Biophys. Mol. Biol.* **2008**, *97*, 163−179.
(59) Daniele, M. A.; Adams, A. A.; Naciri, J.; North, S. H.; Ligler, F. S. Interpenetrating Networks Based on Gelatin Methacrylamide and PEG Formed Using Concurrent Thiol Click Chemistries for Hydrogel Tissue Engineering Scaffolds. *Biomaterials* **2014**, *35*, 1845−1856.
(60) Heer, N. C.; Martin, A. C. Tension, Contraction and Tissue Morphogenesis. *Development* **2017**, *144*, 4249−4260.
(61) Zhao, R.; Chen, C. S.; Reich, D. H. Force-Driven Evolution of Mesoscale Structure in Engineered 3D Microtissues and the Modulation of Tissue Stiffening. *Biomaterials* **2014**, *35*, 5056−5064.
(62) Sanz-Moreno, V.; Gaggioli, C.; Yeo, M.; Albrengues, J.; Wallberg, F.; Viros, A.; Hooper, S.; Mitter, R.; Féral, C. C.; Cook, M.; et al. ROCK and JAK1 Signaling Cooperate to Control Actomyosin Contractility in Tumor Cells and Stroma. *Cancer Cell* **2011**, *20*, 229−245.
(63) Sweeney, H. L.; Hammers, D. W. Muscle Contraction. *Cold Spring Harbor Perspect. Biol.* **2018**, *10*, a023200−a023213.
(64) Thibeault, S. L.; Klemuk, S. A.; Chen, X.; Johnson, B. H. Q. In Vivo Engineering of the Vocal Fold ECM with Injectable HA Hydrogels—late Effects on Tissue Repair and Biomechanics in a Rabbit Model. *J. Voice* **2011**, *25*, 249−253.
(65) Brown, R. D.; Ambler, S. K.; Mitchell, M. D.; Long, C. S. The Cardiac Fibroblast: Therapeutic Target in Myocardial Remodeling and Failure. *Annu. Rev. Pharmacol. Toxicol.* **2005**, *45*, 657−687.
(66) Ghilardi, S. J.; O'Reilly, B. M.; Sgro, A. E. Intracellular Signaling Dynamics and Their Role in Coordinating Tissue Repair. *Wiley Interdiscip. Rev.: Syst. Biol. and Med.* **2020**, *12*, e1479−e1504.
(67) Li, B.; Wang, J. H.-C. Fibroblasts and Myofibroblasts in Wound Healing: Force Generation and Measurement. *J Tissue Viability* **2011**, *20*, 108−120.

https://dx.doi.org/10.1021/acssensors.0c02172
ACS Sens. 2021, 6, 985−994